Journal of Materials Chemistry C

PAPER

View Article Online
View Journal | View Issue

Cite this: J. Mater. Chem. C, 2016, 4, 5795

Nine-ring angular fused biscarbazoloanthracene displaying a solid state based excimer emission suitable for OLED application†

Gleb V. Baryshnikov,‡[ab] Pawel Gawrys,‡*[c] Khrystyna Ivaniuk,[d] Bernhard Witulski,*[e] Richard J. Whitby,*[c] Ayham Al-Muhammad,[c] Boris Minaev,[a] Vladyslav Cherpak,[d] Pavlo Stakhira,[d] Dmytro Volyniuk,[f] Gabriela Wiosna-Salyga,[g] Beata Luszczynska,[g] Algirdas Lazauskas,[h] Sigitas Tamulevicius[h] and Juozas V. Grazulevicius[f]

A new biscarbazoloanthracene consisting of nine fused aromatic rings, including two pyrrole units, has been obtained in a straightforward and convergent synthesis. Computational chemistry and conformational analysis revealed that the semiconductor's molecule is not planar, the two carbazole moieties being helical twisted from the plane of the anthracene unit. Photophysical and electrochemical measurements showed that this angular fused heteroacene has a low lying HOMO energy level with a wide band gap despite its extended π-conjugated molecular framework. Based on its relatively low-lying HOMO level, the semiconductor promises a high environmental stability in comparison to other related linear fused acenes and heteroacenes. The biscarbazoloanthracene has been applied as the light emitting layer in a white light emitting diode (WOLED). It is proposed that the white OLED feature is due to dual light emission properties from the active semiconductor layer being based on both the molecular luminescence of the small molecule and a discrete excimer emission made possible by suitable aggregates in the solid state. Noteworthy, this is the first reported example of such a behavior observed in a small molecule heteroacene rather than an oligomer or a polymer.

Received 11th April 2016,
Accepted 23rd May 2016

DOI: 10.1039/c6tc01469k

www.rsc.org/MaterialsC

Introduction

The molecular structure of π-extended aromatic or heteroaromatic compounds, together with their molecular packing in the solid state, govern to a great extent the physical properties of the resulting semiconducting films. This includes absorption and luminescence behaviour, conductivity, and charge carrier mobility, *etc.* In this context, the formation of excimers (excited-state dimers) that is favoured by certain molecular aggregates formed in films or crystalline domains, seems to be an effective tool to tune the colour of emitted light from an OLED. Notably, excimer formation is characterized by a broad and structureless long-wavelength band in the photo- or electroluminescence spectra, relative to the emission spectra of the single molecule. As the broad excimer emission in solid films is often accompanied by luminescence properties based on the single molecule such dual emission properties can be used as an efficient tool for light management resulting in white light emission. Recently, this concept has been used for the fabrication of excimer- (or exciplex)-based white-light emitting OLEDs which contain only a single light emitting layer.[1] However, it should be noted that excimer formation is accompanied by a decrease of the luminescence quantum yield due to the increase of non-radiative decay processes.[2] Nonetheless, the presence of molecular aggregates that favour excimer formation will also support the enhancement of charge transport properties[3] due to specific restrictions on intramolecular rotations.[4] Considering these antagonistic factors, there is an urgent need for integrated studies of organic semiconductors that are characterized by the presence of

[a] Bohdan Khmelnytsky National University, Shevchenko 81, 18031 Cherkassy, Ukraine
[b] Division of Theoretical Chemistry and Biology, School of Biotechnology, KTH Royal Institute of Technology, 10691 Stockholm, Sweden
[c] Chemistry, University of Southampton, Southampton, SO17 1BJ, UK. E-mail: majdo007@wp.pl, rjw1@soton.ac.uk
[d] Lviv Polytechnic National University, S. Bandera 12, 79013 Lviv, Ukraine
[e] Laboratoire de Chimie Moléculaire et Thioorganique, UMR 6507 CNRS, Normandie University, ENSICAEN & UNICAEN, 6 Bvd du Marechal Juin, 14050 Caen, France. E-mail: bernhard.witulski@ensicaen.fr
[f] Department of Polymer Chemistry and Technology, Kaunas University of Technology, Radvilenu Plentas 19, LT-50254, Kaunas, Lithuania
[g] Department of Molecular Physics, Lodz University of Technology, Zeromskiego str.116, 90-924 Lodz, Poland
[h] Institute of Materials Science, Kaunas University of Technology, Baršausko str. 59, LT-51423 Kaunas, Lithuania

† Electronic supplementary information (ESI) available: Synthesis and spectra of new compounds, additional theoretical and device data. See DOI: 10.1039/c6tc01469k

‡ These authors contributed equally to this work.

excimer emission. Here, we report on 10,20-didodecyl-5,15-bis(2-ethyl-1-hexyl)biscarbazolo[3,4-*a*:3′,4′-*h*]anthracene (**3**), a compound which possesses a strong dual emission behaviour in solid films that is due to excimer formation. In this paper we present a first synthesis, experimental and theoretical data on the molecular structure of **3**, its absorption and luminescence spectra in solution and solid state as well as its charge carrier transport properties in films of vacuum deposited **3**. Furthermore the novel emitter was used for the fabrication of a white OLED.

Experimental methods

Optical measurements

UV absorption spectra in solution were recorded with a JASCO V-660 spectrometer and emission spectra with a Perkin Elmer LS55 fluorescence spectrometer. Absolute photoluminescence quantum yields as well as luminescence spectra of solids and in solution were recorded with the Hamamatsu CC9920 integration sphere set-up at room temperature. For quantum yield measurements solutions of **3** were purged with argon prior to measurement. Luminescence spectra, quantum yields and decay curves of vacuum deposited films of **3** were recorded with the Edinburgh Instruments FLS980 spectrometer at room temperature using EPLED 340 nm picosecond pulsed light emitting diode as the excitation source.

Electrochemistry

Electrochemical studies were carried out at room temperature using a GAMRY Ref600 potentiostat. The working electrode was a platinum electrode, the auxiliary electrode a platinum wire. The reference electrode was an aqueous saturated (KCl) calomel electrode. Under the conditions used, the reversible potential for the ferrocenium/ferrocene couple at 298 K is +0.46 V in CH_2Cl_2. Solutions of **3** (0.5×10^{-4} M) in a 1×10^{-1} M Bu_4NPF_6/CH_2Cl_2 electrolyte solution were used.

Thermal properties

TGA measurements were recorded on a Perkin Elmer Thermogravimetric Analyser TGA7. Differential Scanning Calorimetry measurements were performed on a Perkin Elmer DSC7 analyser.

Photoelectrical properties

The ionization potential (IP) of the layers of **3** was measured by the photoelectron emission method in the air.[5] The samples were fabricated by vacuum deposition of compound **3** onto indium tin oxide (ITO) coated glass substrate. The experimental setup consisted of the deep-UV deuterium light source ASBN-D130-CM, the CM110 1/8 m monochromator, and the 6517B Keithley electrometer.

Mobility of the thin layers

The time of light (TOF) method was used for the investigation of the charge carrier mobility properties. For this purpose vacuum deposited layers of **3** onto ITO coated glass were coated by evaporated aluminum (Al) top-contacts. Individual samples had areas of 0.06 cm^2. For the TOF measurements a pulsed third-harmonic Nd:YAG laser EKSPLA NL300 working at a pulse duration of 3–6 ns and a wavelength of 355 nm was used. A 6517B Keithley electrometer was used to apply direct positive voltage to the ITO. The TOF signal was recorded by a digital storage oscilloscope Tektronix TDS 3032C.

XRD of the thin layers

The XRD properties of **3** in the solid state, were recorded using thin layers deposited under vacuum onto pre-cleaned quartz substrates. X-ray diffraction measurements at grazing incidence (XRDGI) were performed using D8 Discover diffractometer (Bruker) with Cu Kα (λ = 1.54 Å) X-ray source. Parallel beam geometry with 60 mm Göbel mirror (X-ray mirror on a high precision parabolic surface) was used. It transforms the divergent incident X-ray beam from a line focus of the X-ray tube into a parallel beam that is free of Kβ radiation. Primary side also had a Soller slit with an axial divergence of 2.5°. The secondary side had a LYNXEYE (0D mode) detector with an opening angle of 1.275° and slit opening of 9.5 mm. Sample stage was a Centric Eulerian cradle mounted to horizontal D8 Discover with a vacuum chuck (sample holder) fixed on the top of the stage. X-ray generator voltage and current was 40.0 kV and 40 mA, respectively. XRDGI scans were performed in the range of 3.0–135.0° with step size of 0.066°, time per step of 0.1 s and auto-repeat function enabled. Processing of the resultant diffractogram was performed with DIFFRAC.EVA software.

Morphology

Surface morphology of vacuum deposited films of **3** was investigated using atomic force microscopy (AFM). AFM experiments were carried out in air at room temperature using a NanoWizard III atomic force microscope (JPK Instruments), while data was analyzed using SurfaceXplorer and JPKSPM Data Processing software. The AFM images were collected using a V-shaped silicon cantilever (spring constant of 3 N m^{-1}, tip curvature radius of 10.0 nm and the cone angle of 20°) operating in a contact mode.

Electroluminescence and OLEDs

The electroluminescent device was fabricated by deposition of organic semiconductor layers (at 150 °C) and metal electrodes onto pre-cleaned ITO-coated glass substrate under a vacuum of 10^{-5} Torr. The device was fabricated through the step-by-step deposition of various functional layers. CuI and 4,7-diphenyl-1,10-phenanthroline (Bphen) compounds were used for the hole- and electron-transporting layers, respectively.[6] A Ca layer topped with aluminum (Al) was used as the cathode. The Bphen is a well-known hole blocking layer and electron transporting material[7] being widely used to promote electron transfer from the Ca:Al cathode to the central emissive layer. The structure of the fabricated device was as follows: ITO/CuI(8 nm)/**3**(40 nm)/Bphen(10 nm)/Ca(50 nm):Al(200 nm). The active area of the obtained device was 3×6 mm^2. Characteristics of the current density–voltage and luminance–voltage dependencies were measured with a semiconductor parameter analyzer (HP 4145A) in air without passivation immediately after fabrication of the device. The measurement of brightness was performed using a

calibrated photodiode. The OLED electroluminescence and PL spectra of the solid films were recorded with an Ocean Optics USB2000 spectrometer.

Computational details

The ground singlet-state geometry of molecule **3** was optimized at the B3LYP/6-31G(d)[8] level of density functional theory (DFT) using the Gaussian 09 software package (Revision C.02).[9] All the calculated vibration frequencies were found to be real, which indicated the finding of a true energy minimum on the potential energy hypersurface. Using the time-dependent (TD) DFT method,[10] 30 singlet–singlet electronic transitions were calculated using the polarizable continuum model (PCM) for solvation[11] with chlorobenzene as a solvent (as used in the experimental absorption spectra of **3**). The profiles of calculated electronic absorption spectra curves have been simulated with the SWizard program[12] using the Gauss line shape (with a line half-width of 1000 cm^{-1}). Reorganization energy values for the electron (λ_-) and hole (λ_+) carriers have been calculated using the following equation being widely used for estimation of the charge transport properties of organic materials:[13]

$$\lambda_{-/+} = (E_{-/+}^{*} - E_{-/+}) + (E_{-/+}^{**} - E_0), \quad (1)$$

where E_0 is the optimized ground state energy of **3** neutral molecule, $E_{-/+}$ is the energy of the optimized **3** anionic/cationic species, $E_{-/+}^{**}$ is the energy of the neutral molecule at the anionic/cationic geometry and $E_{-/+}^{*}$ is the energy of the anionic/cationic molecule at the optimized geometry of the neutral species. Calculations on the cyclisation of 4 used DFT calculations at the B3LYP/6-31G(d) level using a PCM model for DMF to simulate the NMP solvent.[9] All calculations were performed on the PDC supercomputers of the Royal Institute of Technology, Stockholm.

Results and discussion

Synthesis

The biscarbazoloanthracene **3** was prepared *via* a bidirectional synthesis starting from readily available 1,4-dibromo-2,5-diiodobenzene (see Scheme 1 and ESI†).[14] Sonagashira coupling of 1,4-dibromo-2,5-diiodobenzene with two equivalents of 1-tetradecyne gave the dibromide **1** in 85% yield after its isolation by column chromatography. The cross-coupling reaction is highly selective as it preferentially occurs at the iodine moieties of 1,4-dibromo-2,5-diiodobenzene. Double Suzuki coupling of **1** with *N*-(2-ethyl)hexyl-3-carbazoleboronic acid[15] gave the bis-carbazoyl **2** in high yield. Finally, the DBU catalysed double isomerisation-cycloaromatisation cascade[16,17] of **2** resulted in the construct of the polycyclic aromatic **3** as the major product. Compound **3** was accompanied by a small amount of the non-symmetric by-product (**3′**), easily removed by crystallisation. The structure of **3** was confirmed by NMR and MS spectroscopy. In particular a 9 Hz coupling between Ha and Hb in the ^{1}H NMR spectra distinguished **3** from alternative possible cyclisation products. The presence of **3′** (~5%) in the product mixture was suggested

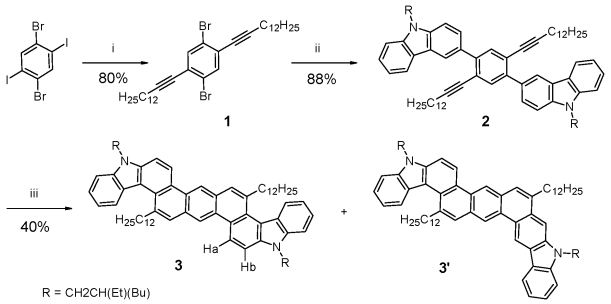

Scheme 1 Synthetic path to **3** (full scheme in ESI†). (i) 2 eq. 1-tetradecyne, $PdCl_2(PPh_3)_2$ (12%), CuI (6%) in NEt_3/DMF (2 : 1), 20 °C, 86 h; (ii) $PdCl_2(PPh_3)_2$, 2.5 eq. 9-(2-ethyl-1-hexyl)-3-carbazolyl boronic acid, 4 eq. Na_2CO_3, THF/H_2O (4 : 1), 6 h, reflux (iii) DBU, NMP, 202 °C, 3 days.

by singlets at 9.65 and 9.30 ppm in the ^{1}H NMR. The selectivity preference for cyclisation to the 3,4-bond of the carbazole – rather than the 2,3-bond – is notable, particularly, as the aromatic compound formed is the less stable product due to steric interactions which twist the aromatic molecular skeleton (see below).

The underlying isomerisation-cyclisation reaction was investigated on a model system **4** (Scheme 2) using DFT calculations. The key step is the $6e^-$ electrocyclic ring closure of allene **4** resulting from a base catalysed isomerisation of the starting alkyne.[18] We found that the activation energy for the cyclisation of **4** to give **6** was 9 kJ mol^{-1} lower than that leading to **6′**. It is interesting to note that **6** is more stable than **6′**, but after the final aromatisation step (*via* deprotonation/reprotonation) the intrinsic stability is reversed (**7′** 43.5 kJ mol^{-1} lower energy than **7**). Chemically, the observed selectivity can be understood by retention of the pyrrole ring aromaticity in **TS-5**, but not in **TS-5′**.

Structure characterisation

With the aim to increase the solubility of the final fused 9-ring heteroacene **3**, the 2-ethylhexyl group on each of the carbazole

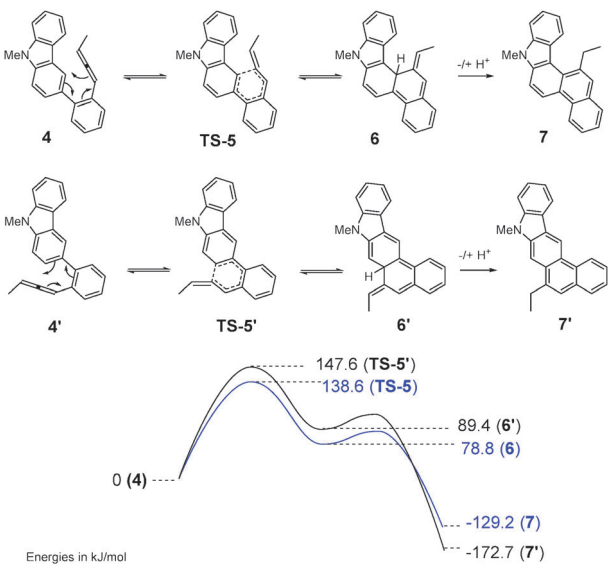

Scheme 2 Alternative cyclisation pathways. The energies given are the calculated Gibbs free energies at 202 °C in kJ mol^{-1}.

nitrogens was used – although this results in the formation of diastereomers of the final product. Gratifyingly, heteroacene **3** has a good solubility in chlorinated solvents, alkylbenzenes, ether solvents and warm hexane, although not soluble in methanol or ethanol. Because the stereocenters of the 2-ethylhexyl groups are far apart from each other, the signals observed on NMR spectra from those diastereoisomers are isochronous.[19]

Quantum chemical calculations allowed the prediction of the geometry of **3** including characterisation of the molecular conformation and bond lengths. In these studies **3** was modelled with methyl groups replacing the two 2-ethylhexyl and two *n*-dodecyl groups for simplicity and to keep computational time reasonable (Fig. 1a). The structural analysis indicates that **3** can adopt two major conformers. One of them is a "chair-like" conformer, in which one of the carbazole units is bent up and the second one bent down – with respect to the flat central anthracene unit (Fig. 1b). The second conformer is "boat-like" and here both carbazole moieties are tilted in the same direction by $\sim 20^{\circ}$ with respect to the anthracene unit (Fig. 1d).

The B3LYP/6-31G(d) optimized "chair-like" and "boat-like" structures of **3** are presented in Fig. 1 in the top and side projections. The total energy of the "chair-like" conformer is only 2.6 kJ mol^{-1} lower in energy than the "boat-like" form. In order to estimate the "chair-boat" transformation the transition-state structure for such an interconversion process was optimized (Fig. 1c).[20] The TS energy is only 17.7 kJ mol^{-1} above the energy of the more stable "chair-like" isomer. Such a low TS energy for an interconversion process suggests a rapid dynamic equilibrium between the two conformers in solution at room temperature.[21]

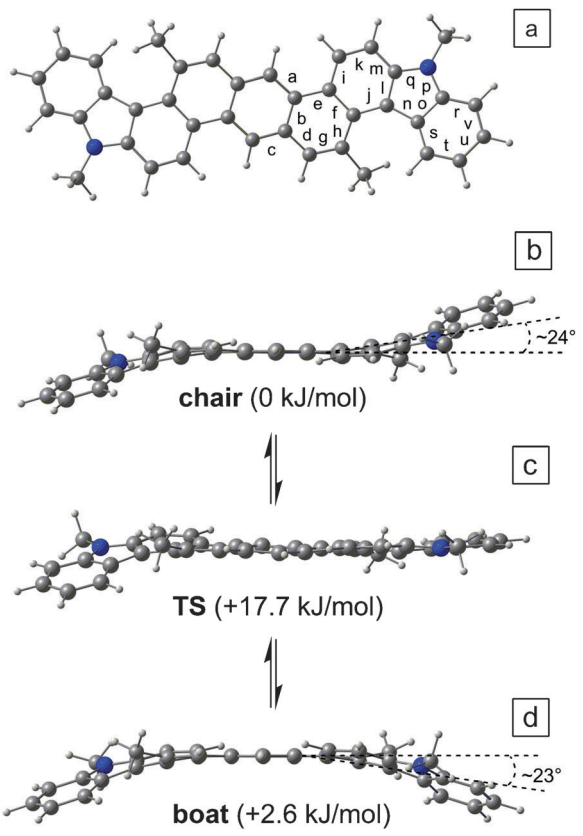

Fig. 1 The B3LYP/6-31G(d) optimized structure of the **3** molecule (methyl groups used for clarity): (a) top view of both boat and chair isomers; (b) side view of chair isomer, (c) transition state for the "chair-boat" interconversion, (d) side view of "boat" isomer. Bond lengths are in the Table S1 (ESI†).

Thermal properties

The thermal properties of **3** were investigated by thermogravimetric analysis (TGA) and differential scanning calorimetry (DSC). Based on the TGA analysis **3** is thermally stable up to 430 °C under a nitrogen atmosphere. The following decomposition process was completed when the temperature was raised above 670 °C. Thermal transitions of **3** have been studied by DSC. After a first heating/cooling cycle the compound remains in a glassy state without significant crystallisation. However, in the second heating/cooling cycle the exothermic transition at T_c = 68 °C indicates a solid to solid transition, that implies conformational changes to a more favourable solid state molecular packing, and it was followed by a endotherm melting at T_m = 107 °C (for TGA and DSC plots, see ESI†).

Electrochemical properties

Cyclic voltammetry experiments with **3** were carried out in the presence of Bu_4NPF_6 (0.1 M in CH_2Cl_2) with Fc*/Fc*$^+$ (−0.13 V *vs.* SCE)[22] as the internal standard.[23] Within the solvent/electrolyte window **3** showed two quasi reversible oxidation waves at $E^{ox}_{1/2}$(I) = 0.87 V and $E^{ox}_{1/2}$(II) = 1.27 V, respectively (Fig. 2). From the onset of the first oxidation half-wave E^{ox}_{onset}(I) = 0.82 V, the energy level of the highest occupied molecular orbital (HOMO) **3** was estimated at E(HOMO) = −5.46 eV with $E_{HOMO} = -(E_{onset,ox\ vs.\ Fc/Fc^+} + 5.1\ (eV))$ for measurements in dichloromethane solution with 0.1 M Bu_4NPF_6 as the supporting electrolyte.[24] This HOMO energy level is lower than those for the 5-ring fused heteroacene 5,11-dimethylindolo[3,2-*b*]carbazole (−5.32 eV)[25] and our recently disclosed heptacene-type structures of the linear fused 5,8,14-tri-*n*-hexyldiindolo[3,2-*b*;2′,3′-*h*]carbazole (−5.06 eV)[26] and the angular fused bis[1,2-*a*:1′,2′-*h*]indoloanthracene (−5.23 eV).[27] Notably, the experimentally determined E_{HOMO} energy of **3** is remarkably low for such a highly extended π-conjugated

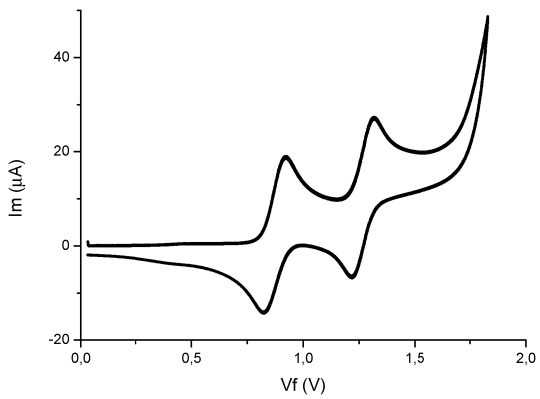

Fig. 2 Cyclic voltammetry curve of **3** (8×10^{-4} M in CH_2Cl_2/0.1 M *n*-Bu_4PF_6) at room temperature. Scan rate 100 mV s^{-1}, values are corrected *vs.* internal Fc* (−0.13 V *vs.* SCE).

molecular scaffold containing nine rings and it emphasizes a better oxidation stability of **3**.

The energy level of the lowest unoccupied molecular orbital (LUMO) was estimated by adding the value of the optical band gap taken from the onset of the absorption spectra of **3** in chlorobenzene (λ_{onset} = 450 nm, 2.76 eV) to the E_{HOMO} providing E_{LUMO} = −2.70 eV. This quite low value of the LUMO level is similar to the values reported for extended carbazoles,[28] indenofluorenes,[29] triarylamine capped polyaromatic hydrocarbons[30] or others.[31] The consequence for such LUMO level, lying clearly below −2 eV, should be an easier electron injection from the cathode during the device operation.[32]

Photoelectrical properties

The ionization potential (I_p) of the solid film of **3** was estimated from the photoelectron emission spectra (ESI†). Notably, the value of I_p (5.35 eV) of **3** is in a good agreement with the 'electrochemical' HOMO level (−5.46 eV). This relatively high I_p value also indicates that films of **3** should be efficient at accepting holes injected from the anode.[33]

Computational results

The DTF calculated energy of the HOMO and LUMO orbitals (Table 1) are overestimated compared to the electrochemically determined values. The overestimation of the LUMO level is more significant and aiding this would require using much more complex basis sets.[34] This is a known limitation of DFT theory but the usual deviations from the experimental data are not critical for the correct analysis of molecular energy level. The theoretical and the experimental results qualitatively agree that **3** represents wide-bandgap semiconducting materials.

The frontier HOMO/LUMO orbitals for the 9-ring fused heteroacene **3** are presented in Fig. 3. Both orbitals represent the π-type wave-functions localized predominantly on the central anthracene unit with only the a minor contribution from the carbazole moieties. The shape of the HOMO orbital of **3** is quite similar to that of the parent anthracene, while the LUMO orbital of **3** is rather different because of the distortion of bonding function in the $C_\alpha CCC_\alpha$ chain of each benzene ring.

Optical and photophysical properties

The experimental absorption spectra of compound **3** measured for the solid film state and in chlorobenzene solution, together with the TD DFT calculated curve, are presented in Fig. 4. The absorption spectrum in the solid film possesses a small bathochromic shift relative to the solution spectrum. These effects can be associated with the formation of the aggregates which probably correspond to a "plane-to-plane" π-stacked type coupling.[35]

Table 1 Energies of frontier molecular orbitals of **3**, calculated by DFT B3LYP/6-31G(d) method and determined by cyclic voltammetry and UV-vis spectroscopy

3	E_{HOMO} (eV)	E_{LUMO} (eV)	HOMO/LUMO gap (eV)
Experimental	−5.46	−2.70	2.76
Calculated	−4.79	−1.42	3.37

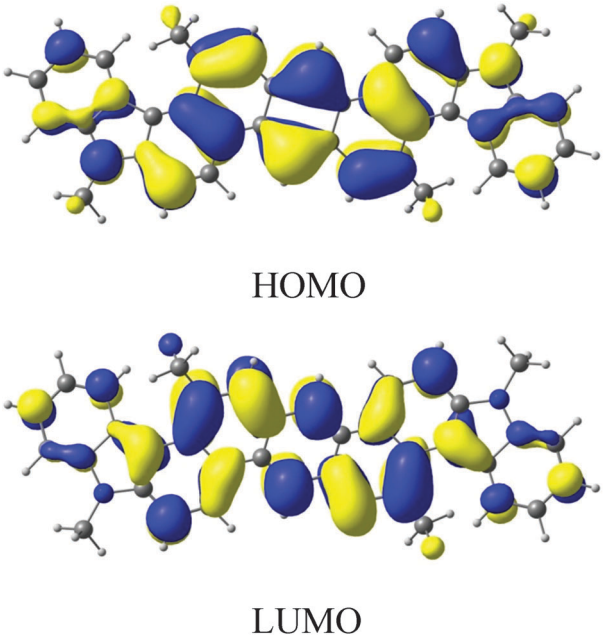

Fig. 3 Frontier molecular orbitals of **3** for the "chair-like" conformer calculated with the B3LYP/6-31G(d) method (identical plots were obtained for the "boat-like" isomer, see ESI†). Methyl groups were used for simplicity.

The correlation between the experimental and calculated spectra is very good. However, one has to consider that vibronic satellite peaks cannot be accounted in the vertical TD-DFT approximation that was used here.[36]

The first absorption band in the experimental spectrum of **3** in chlorobenzene is positioned at 438 nm. This band, calculated at 426 nm, corresponds to the first singlet–singlet symmetry allowed HOMO–LUMO electronic transition (Fig. 4 and Table 2). The second broad absorption band at 409 nm is interpreted as the HOMO−1 → LUMO electronic transition with a small part of HOMO → LUMO+2 excitation. This transition is about three times more intense than $S_0 \rightarrow S_1$ transition. The two broad shoulders at about 365 and 380 nm can be assigned to the vibronic progression of the $S_0 \rightarrow S_2$ transition. The intense absorption maximum at 350 nm corresponds to the ππ*-electronic transition

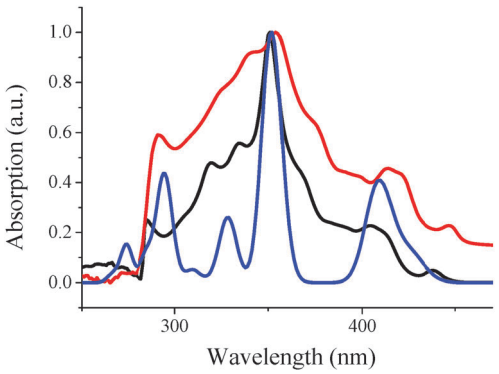

Fig. 4 Normalized absorption spectra of **3** for solid films (red), as well as of the **3** in chlorobenzene (black, 10^{-6} M) and the TD-DFT/B3LYP/6-31G(d) simulated curve using the PCM approach (blue).

Table 2 Calculated energy, oscillator strength (f) and orbital assignment of the singlet–singlet vertical electronic transitions for the **3** molecule

State	λ, nm	λ_{exp}, nm	f	Assignment
S_1	425.6	438[a] (448[b])	0.1831	HOMO → LUMO (93%)
S_2	408.9	405[a] (414[b])	0.6553	HOMO−1 → LUMO (86%) HOMO → LUMO+2 (8%)
S_5	351.8	350[a] (354[b])	1.6361	HOMO → LUMO+2 (87%) HOMO−1 → LUMO (10%)
S_8	328.5	333[a]	0.4214	HOMO−1 → LUMO+2 (81%)
S_9	321.4	(341[b])	0.0188	HOMO−5 → LUMO (75%)

[a] Chlorobenzene solution. [b] Solid film.

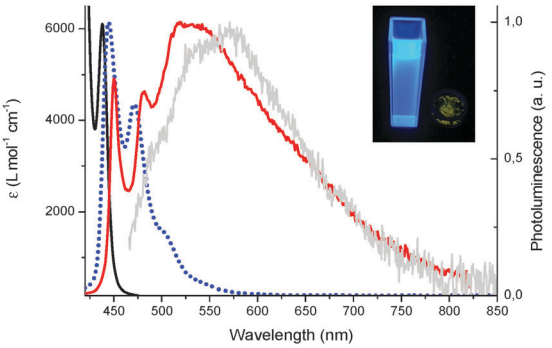

Fig. 5 Absorption (black) and photoluminescence spectra (λ_{ex} = 350 nm) of **3** in chlorobenzene (10^{-6} M) (dotted blue), vacuum-deposited solid film (red), and solid state luminescence spectra of crystalline **3** (grey). Inset, **3** in solution and solid under UV-light.

calculated to be at 352 nm. This transition is also vibronically active and a vibronic satellite peak is resolved at 378 nm. Some high-energy electronic bands below 350 nm, noted in the experimental and calculated spectra, are less significant for the functional properties of **3**.

The three-band model of absorption spectrum is applicable here. In anthracene the first p-band (S1 state) is weak, the second (α-band) is almost forbidden and the third (β-band) is most intensive in the spectrum. In **3**, the α-band is quite intense because the corresponding orbitals which form the S2 state are significantly delocalized over the whole molecule (ESI†). In shorter bisindoloanthracene, this effect is not so pronounced.[27] All the p-(S1), α-(S2) and β-(S5) have in-plane polarization usual for the ππ*-states. The differences in the observed intensities are caused only by the symmetry and shape of the corresponding MOs wavefunctions. In comparison to anthracene, the expansion provides a red-shift of the whole absorption spectrum (due to the common phenomenon of electron correlation) and strong enhancement of the α-band.

In order to evaluate luminescence performance of **3** we have recorded its fluorescence spectra in solution and solid state (Fig. 5). The photoluminescence spectrum of **3** dissolved in chlorobenzene is characterized by two high-energy bands observed at 445 nm and 470 nm being responsible for the bright blue colour of light emission. Furthermore, the small Stokes shift of 6 nm with respect to the absorption corresponding to the $S_0 \rightarrow S_1$ transition and the solution quantum yield of Φ_F = 49% (λ_{ex} = 350 nm) for **3** (10^{-6} M in chlorobenzene) indicate the rigidity of the heteroaromatic core. The solid state emission of **3** (crystals) is characterized by a broad structureless band with a maximum at about 570 nm with a corresponding quantum yield of Φ_F = 4% (λ_{ex} = 350 nm) that is significantly lower compared to that of **3** in solution.

Vacuum-deposited films of **3** are also characterized by a broad emission (Φ_F = 6%, λ_{ex} = 350 nm) with a low-energy band with a maximum around 530 nm besides the two additional high-energy maxima at 450 nm and 480 nm. Notably, the photoluminescence spectra of the film and crystals of **3** show comparable broad emission bands at low energy that both tail-off at about 800 nm. With respect to the high-energy bands of the photoluminescence spectra of **3** in solution, the two related high-energy bands of the vacuum deposited film emission spectra are red shifted by approximately 10 nm. This red shift is apparently caused by both the negligible reabsorption of fluorescence and by the slight reciprocal influence of neighbouring molecules the in solid films.[37]

The broad structureless emission in the PL spectrum of **3** in both crystals and solid films, and with similar tail-off values at around 800 nm, can be explained most likely by the formation of excited state dimers (excimer).[38] The π-extended framework of **3** which consists of nine aromatic/heteroaromatic rings is considered of being capable to form intramolecular π-aligned complexes favouring such excimer formation. This finding is also support by the fact that the emission spectra of crystals of **3** is exclusively characterised by such an excimer emission due to the regular assembly of molecules in crystals, whereas the vacuum deposited film of **3** shows both, the emission characteristic of isolated molecules, and the excimer emission originated of a certain regular molecular alignment or assembly (see also XRD section below).

Further support of potential excimer formation is provided by the photoluminescence studies of 2-(4-*tert*-butylphenyl)-5-(4-biphenylyl)-1,3,4-oxadiazole (PBD) blends with various concentrations of heteroacene **3**. As excimer formation is concentration dependent, the intensity of the excimer emission is expected to increase with the concentration of the emitter in solution or (PBD) blend. Indeed, with the increment of the **3**:PDB ratio, the broad band between 500–800 nm that is associated with the excimer emission increases as shown in Fig. 6. Additionally we noted the drastic drop of the quantum yield from 18% for a blend containing 5% of **3** in PBD/polyvinylcarbazole (PVK) film to below 2% for solution deposited thin films of **3**.

The transient recorded at photoluminescence band 450 nm has single-exponential decay profile with the decay time constant (τ) of 1.14 ns, that can be assigned to the **3** exciton fluorescence (Fig. 7 and Table 3).[39] The lower energy emissions (520 and 550 nm) decay with significantly lower half-life times and the decay curves are not anymore monoexponential functions (Fig. 7 and Table 3). Notably, this non-monoexponential character of the decay at 520 and 550 nm respectively indicates the presence of excited states of different nature, for example of long lived excimers.[40]

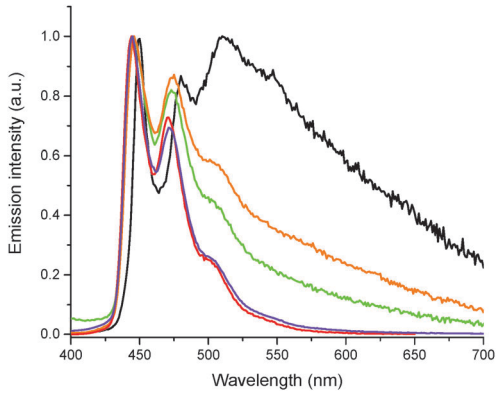

Fig. 6 Photoluminescence spectra of blends of **3** and comparison with solid/solution spectra (λ_{ex} = 350 nm): spin-coated (chlorobenzene) thin film of **3** (black); **3**:PBD 1:1 film (orange); **3**:PBD 1:2 film (green) and **3** (5%) in PVK:PBD film (violet), chlorobenzene solution of **3** (red).

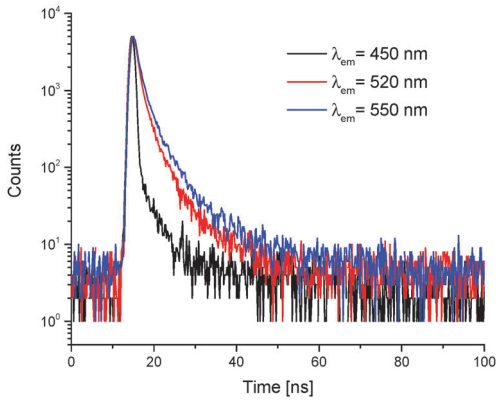

Fig. 7 The fluorescence decay of the films of **3** measured at the different wavelengths: 450, 520, and 550 nm.

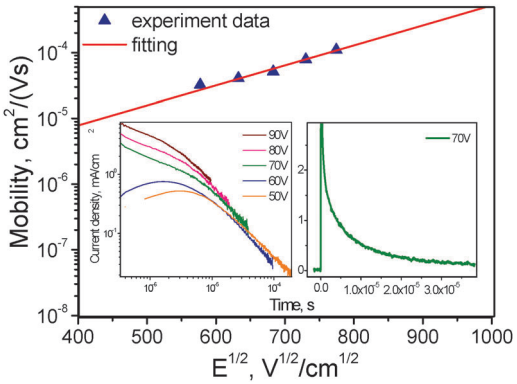

Fig. 8 Electric field dependencies of hole-drift mobility of the **3** compound measured by TOF methods. Inserts: current transient curves of the **3** compounds at different applied voltages in log–log scales and a current transient curve at voltage of 70 V in liner scales.

Charge transport properties

In order to determine the efficiency of films of **3** as the transport layer, estimation of the charge-transport properties of **3** was carried out. The solid films of **3** have a hole mobility in the range from 2.8×10^{-5} to 1.1×10^{-4} $cm^2\ V^{-1}\ s^{-1}$ with fields varying from 3.8×10^5 to 6×10^5 V cm^{-1} (Fig. 8), similarly to one of the recent V-shaped π-extended carbazoles.[41] The experimental data shown on Fig. 8 are well described by equation $\mu = \mu_0 \cdot \exp(\alpha \cdot E^{1/2})$ for the external electric field $E > 0.4 \times 10^5$ V cm^{-1} ($E^{1/2} > 200$ (V cm^{-1})$^{1/2}$), where μ_0 is determined as the zero field electron mobility and α is the field enhancement factor of a Poole–Frenkel type mobility.

Our theoretical DFT predictions of the charge carrier mobility of compound **3** support its good hole-transporting property and suggest reasonable electron-transporting possibilities. The calculated values of the hole and electron reorganization energies (λ_+ and λ_-) are equal to 87 and 274 meV respectively. The lower value of λ_+ indicates a better hole mobility relative to the electron mobility. This conclusion is based on the Marcus theory which describes the theoretical background for the charge carrier mobility.[42]

For the calculation of the hole mobility of **3** the following equation was used: $\mu = d^2/U \cdot t_{tr}$, where d is thickness of the film (1.5 μm), t_{tr} is the transit time, and U is the applied voltage. The transit times were determined from the intersection of the asymptotes to the plateau and tail of the transient signal in the double logarithmic plots. As illustrated (Fig. 8 insets), the tails of the photocurrent transients of **3** indicate the dispersive hole transport of the semiconductor.[43] The moderate mobility as well as dispersive type transport are likely to originate from poor ordering in the thin films of **3**.[44] In agreement with our data below, the thin film of **3** is likely to have crystalline domains well separated by amorphous regions.

X-ray diffraction

To describe the supramolecular organisation of the thin layers of **3** we have performed their X-ray diffraction analysis. In the XRD pattern (ESI†) we observe the narrow high-intensity signal at $2\theta = 5.029^\circ$ which corresponds to the long-range order of the crystals of **3**. The very high inter-plane distance equals to 17.59 Å as derived from the Bragg's law. The next broad reflex at $2\theta = 21.138^\circ$ indicates the presence of the long-range dispersed crystal grains of **3**. The resulting average inter-plane distance of 4.2 Å can be ascribed to the intermolecular distance between the two stacked molecules of **3**. The presence of such dimers may provide the broadening and red shift of the absorption spectrum of the condensed phase of **3** (comparing with the one measured in solution) and facilitate the formation of the excimers

Table 3 Fitting results of the photoluminescence transients of the **3** solid films prepared by vacuum deposition at 300 K

Wavelength of photoluminescence spectra (nm)	450	520	550
Photoluminescence lifetimes (τ) (ns)	1.14 (100%)	5.07 (88%)	7.99 (75%)
		19.2 (12%)	29.7 (25%)
χ^2	1.298	1.267	1.274

which give the long-wavelength structureless emission. The packing in the thin film of **3** is clearly less dense than in the analogous thin layers of bisindoloanthracene.[27] Although the aromatic ribbon here is more extended, the bulkier and longer alkyl groups may provide more significant repulsion between the aromatic planes.

Morphology

AFM measurements were performed on vacuum deposited film of **3** on quartz substrate (ESI†). The topography shows randomly oriented surface morphological features with 2.73 nm of the mean height of the peaks and the root mean square roughness (R_q) of 0.69 nm. The surface of **3** is dominated by the peaks with skewness (R_{sk}) value of 0.23 and has a leptokurtic distribution of the morphological features with kurtosis (R_{ku}) value of 3.30 indicating relatively many high peaks and low valleys.

To assess the morphologic stability of the film, the sample of deposited **3** was kept at room temperature and relative humidity of 40–50% for 10 months and AFM measurement was repeated. In contrast to freshly prepared sample, the topography of aged film of **3** differs mainly by larger size of surface morphological features indicating some degree of aggregation with aging. The mean height of surface peaks was found to be *ca.* 11.42 nm. The surface of the aged film of **3** retained relatively similar features (R_{sk} of 0.54 and R_{ku} of 4.20). The surface roughness R_q increased to 3.27 nm.

Electroluminescent devices

The typical electroluminescence spectrum of the device assembled in the ITO/CuI/**3**/Bphen/Ca:Al configuration is characterized by three distinguishable emission bands (Fig. 9): two at 450 nm and 480 nm which correspond to the **3** exciton emission and intense excimer broad band (520 nm) with a shoulder at 600 nm. Bphen layer provides exclusively the electron-transport function which is evidenced by the absence of the short-wavelength emission bands (390 and 410 nm) being characteristic for the Bphen.[45] The electroluminescence spectrum of the OLED is quite similar to the PL spectrum of the vacuum deposited **3** film (Fig. 5). The lower-energy band of PL spectrum is wider and red shifted in the comparison with EL spectrum. The electroluminescence seems to be weakly affected by the increment of the driving voltage – a small increase of exciton-type emission is noted (Fig. 9).

Interestingly, different EL spectra were obtained for OLEDs based on the spin-coated blends of **3** (ESI†).[46] We observe rather one quite narrow band with maximum at 465 nm with a shoulder at 485 nm. This EL spectrum somewhat resembles PL spectra of **3** dispersed in the PVK/PBD matrix (Fig. 6) which in turn is faithfully resembling purely excitonic emission of diluted solutions of **3**. We note this as a supporting evidence that emission from WOLEDs described in this work is of dual nature from the single layer.

Fig. 10 shows the current density–voltage characteristics and luminance–voltage characteristics of the electroluminescent device. OLED shows a low turn-on voltage (V_{on}) of 6.5 V for electroluminescence (at 2 cd m^{-2}). The device exhibited current

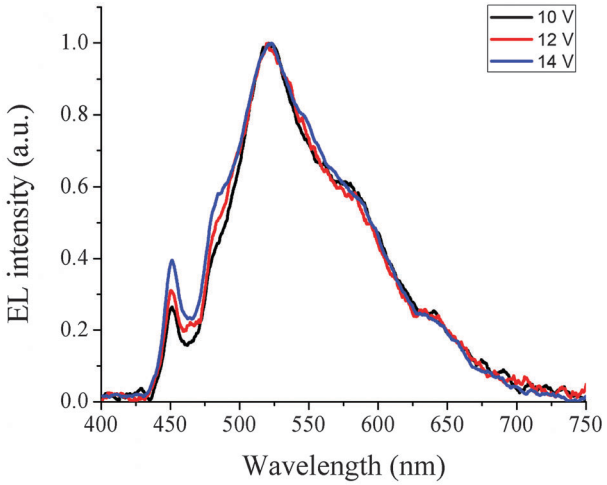

Fig. 9 Electroluminescence spectra of the single-layer OLED of the structure ITO/CuI/3/Bphen/Ca:Al at the different applied voltage.

efficiency values of 3.8 cd A^{-1} and maximum brightness of 2100 cd m^{-2} (at 15 V). Chromaticity coordinates (x, y) of the device were found to be (0.3, 0.43) corresponding to the white color and the temperature of 5500 K (ESI†). The colour rendering index was estimated at 56. The device shows moderate EQE up to 1.3% and power efficiency up to 0.9 lm W^{-1}.

The efficiency of the fabricated OLED is not so high compared with other known OLEDs based on excimer emission,[47] but current efficiency values is high as for many anthracene based fluorescence OLEDs.[48] Despite the fact that the energies of the orbitals of **3** are well fitting *versus* the respective energy levels of ETL and HTL (Fig. 11) some of the OLED parameters might be suppressed due to unbalanced hole and electron recombination[49] or relatively moderate mobility of the thin layer (*vide supra*). Nonetheless we assume that the assembly of the energy levels should diminish the turn on voltage.

To address the issues mentioned in the introduction and correlate them with the device performance it is instructive to remember that because of its molecular structure the supramolecular organisation of **3** features a balance between overlapping of the aromatic planes and repulsion caused by either the substituents or bent and helical structure. The attractive forces are responsible for facilitating excimeric-type emission whereas the repulsive ones prevent complete luminescence quenching, explaining the reasonable luminosity of the derived WOLEDs. Unfortunately this is achieved at the price of lower charge mobility in the thin layers which may affect the current density.

It is difficult to directly compare our results from **3** with other extended fused polyaromatics as they have not so far been used in a single layer-single component WOLEDs. There exist, though, examples when polyaromatic hydrocarbons are used as yellow-orange emitting dopants dispersed in blue emitters (single layer-two components)[50] or mixed with thermally delayed fluorescent emitters.[51] In the first case the devices had impressive luminance but their current and power efficiencies where slightly lower than those of **3** OLEDs. Rubrene seems to be also an excellent material for the doped devices.[52]

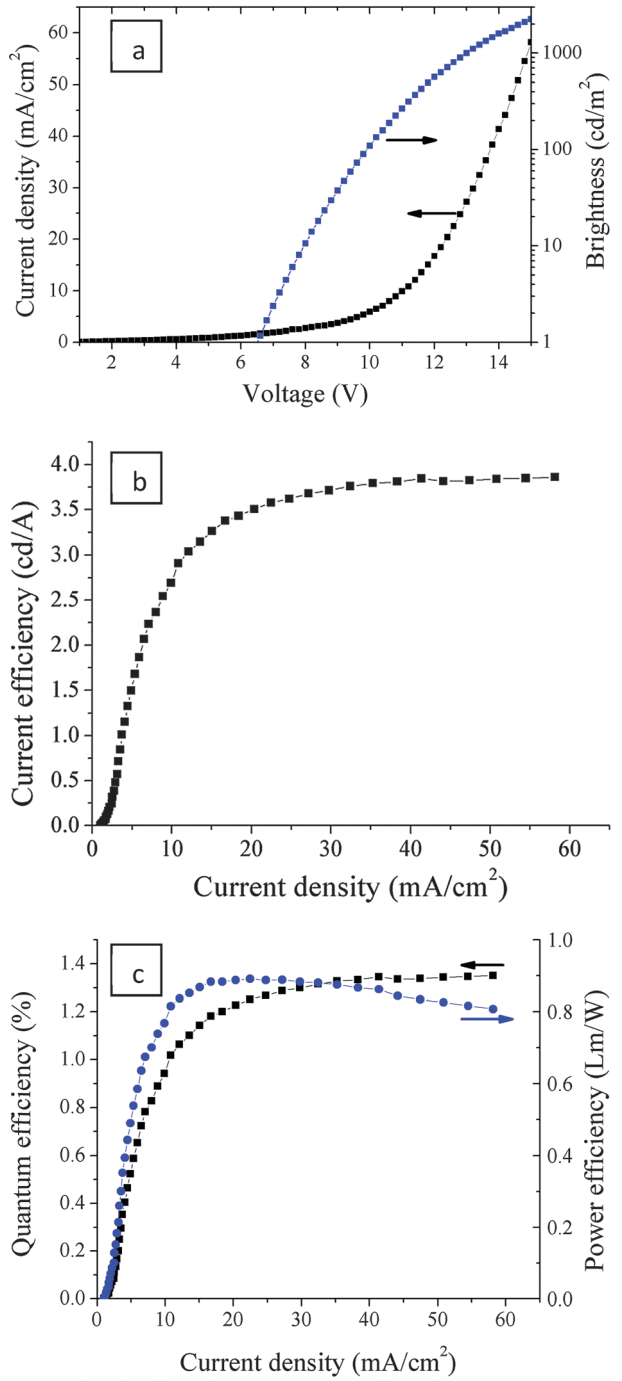

Fig. 10 (a) Current density–voltage and luminance–voltage characteristics, (b) current efficiency–current density characteristic, (c) current density *vs.* power and quantum efficiency characteristics of the fabricated OLED from **3**.

White OLEDs based on single semiconductor layer are rare, especially those of lower molecular weight.[53] For example, 1,3,5-tris(9-(1-naphthyl)anthracen-10-yl)benzene was used for the devices with very similar CIE coordinates to ours.[54]

The phosphorescent single layer-single component WOLEDs have better parameters, however, this class is represented by costly transition metal complexes – mainly platinum based.[53]

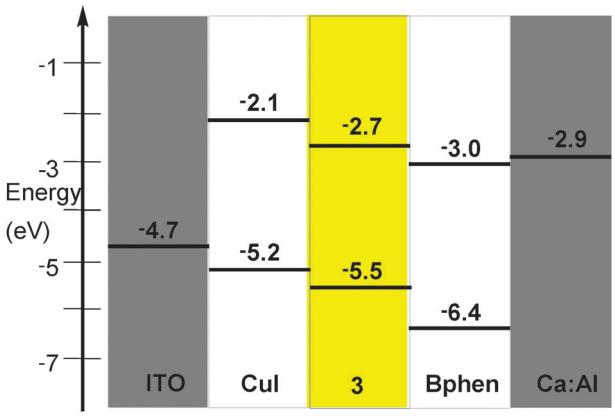

Fig. 11 Energy-band diagrams of the fabricated OLED device incorporating **3**.

Polymeric counterparts are much better studied[53] and even recently an interesting example was introduced.[55] However it seems that their synthesis is much more complex than that of **3**, as there is no need here for asymmetric functionalisation or lengthy synthesis involving tedious copolymer design.

We consider that constructing new polyaromatic moieties and affecting their properties by choosing appropriate alkyl chains is an important area for development.[56] Anthracene and carbazole based materials seem to be primary choices to display interesting phenomena related to luminescence.[57]

Conclusions

We have presented the synthesis and detailed characterisation of a novel biscarbazoloanthracene, a highly soluble extended polyaromatic semiconductor. The new compound displayed very favourable electrochemical properties and sufficient ability to transport hole charge carriers. By comparison of the optical properties in solution and in solid state we proposed an explanation on the photoluminescence spectra of thin films of **3**. Our conclusions, supported with XRD data, suggest that thin layers of **3** may be a source of two different types of emission ascribed to excitons and excimers. This was further evidenced in behaviour of electroluminescent devices based on single (not doped, not blended) layer of **3** whose white emission is best explained as a dual emission from single-component layer. Our results imply that angular polyaromatic compounds with bulky alkyl groups may be applied to fabricate WOLEDs with simple structure.

Acknowledgements

R. J. W., B. W., P. G. and A. A. thank the European Regional Development Fund (ERDF) for funding as part of Interreg IV A projects MEET and IS:CE-Chem. R. J. W., A. A., and P. G. acknowledge EPSRC (UK) core capability funding (EP/K039466). This work was also supported by the Ministry of Education and Science of Ukraine, project no. 0115U003637. G. W.-S. acknowledges the financial support of the National Science Centre (Poland) through the Grant No. 2012/04/S/ST4/00128. This research was

funded by a grant (No. MTEPI-P-16033) from the R&D and Innovation Fund of Kaunas University of Technology. B. Minaev acknowledges the fellowship of Chinese Academy of Science under the CAS President's International Initiative for Visiting Scientists.

References

1 N. Bakken, Z. Wang and J. Li, *J. Photonics Energy*, 2002, **2**, 021203.
2 J. Lee, B. Kim, J. E. Kwon, J. Kim, D. Yokoyama, K. Suzuki, H. Nishimura, A. Wakamiya, S. Y. Park and J. Park, *Chem. Commun.*, 2014, **50**, 14145–14148.
3 (*a*) S. Vasimalla, S. P. Senanayak, M. Sharma, K. S. Narayan and P. K. Iyer, *Chem. Mater.*, 2014, **26**, 4030–4037; (*b*) F. Provencher, N. Bérubé, J.-F. Laprade, G. Simard, J. Tant, V. Halleux, Y. Geerts, C. Silva and M. Côté, *J. Chem. Phys.*, 2012, **137**, 034706.
4 Z. Zhao, S. Chen, J. W. Y. Lam, Z. Wang, P. Lu, F. Mahtab, H. H. Y. Sung, I. D. Williams, Y. Ma, H. S. Kwok and B. Z. Tang, *J. Mater. Chem.*, 2011, **21**, 7210–7216.
5 E. Miyamoto, Y. Yamaguchi and M. Yokoyama, *Electrophotography*, 1989, **28**, 364–370.
6 P. Stakhira, V. Cherpak, D. Volynyuk, F. Ivastchyshyn, Z. Hotra, V. Tataryn and G. Luka, *Thin Solid Films*, 2010, **518**, 7016–7018.
7 M. A. Khan, W. Xu, F. Wei, Y. Bai, X. Y. Jiang, Z. L. Zhang and W. Q. Zhu, *Solid State Commun.*, 2007, **144**, 343–346.
8 (*a*) A. D. Becke, *Phys. Rev. A: At., Mol., Opt. Phys.*, 1988, **38**, 3098–3100; (*b*) C. Lee, W. Yang and R. G. Parr, *Phys. Rev. B: Condens. Matter Mater. Phys.*, 1988, **37**, 785–789; (*c*) M. M. Francl, W. J. Petro, W. J. Hehre, J. S. Binkley, M. S. Gordon, D. J. DeFrees and J. A. Pople, *J. Chem. Phys.*, 1982, **77**, 3654–3665.
9 M. J. Frisch, G. W. Trucks, H. B. Schlegel, G. E. Scuseria, M. A. Robb, J. R. Cheeseman, G. Scalmani, V. Barone, B. Mennucci, G. A. Petersson, H. Nakatsuji, M. Caricato, X. Li, H. P. Hratchian, A. F. Izmaylov, J. Bloino, G. Zheng, J. L. Sonnenberg, M. Hada, M. Ehara, K. Toyota, R. Fukuda, J. Hasegawa, M. Ishida, T. Nakajima, Y. Honda, O. Kitao, H. Nakai, T. Vreven, J. A. Montgomery, Jr.J. E. Peralta, F. Ogliaro, M. Bearpark, J. J. Heyd, E. Brothers, K. N. Kudin, V. N. Staroverov, R. Kobayashi, J. Normand, K. Raghavachari, A. Rendell, J. C. Burant, S. S. Iyengar, J. Tomasi, M. Cossi, N. Rega, M. J. Millam, M. Klene, J. E. Knox, J. B. Cross, V. Bakken, C. Adamo, J. Jaramillo, R. Gomperts, R. E. Stratmann, O. Yazyev, A. J. Austin, R. Cammi, C. Pomelli, J. W. Ochterski, R. L. Martin, K. Morokuma, V. G. Zakrzewski, G. A. Voth, P. Salvador, J. J. Dannenberg, S. Dapprich, A. D. Daniels, Ö. Farkas, J. B. Foresman, J. V. Ortiz, J. Cioslowski and D. J. Fox, *Gaussian 09, Revision C.02 or 2013 Revision D.01*, Gaussian, Inc., Wallingford, CT, 2009.
10 E. Runge and E. K. U. Gross, *Phys. Rev. Lett.*, 1984, **52**, 997–1000.
11 S. Miertus, E. Scrocco and J. Tomasi, *Chem. Phys.*, 1981, **55**, 117–129.
12 S. I. Gorelsky, SWizard Program (Univ. Ottawa, Ottawa, 2013 and 2010); http://www.sg-chem.net/.
13 (*a*) A. Datta, S. Mohakud and S. K. Pati, *J. Chem. Phys.*, 2007, **126**, 144710; (*b*) N. N. Karaush, G. V. Baryshnikov and B. F. Minaev, *Chem. Phys. Lett.*, 2014, **612**, 229–233; (*c*) K. Raghavachari, J. S. Binkley, R. Seeger and J. A. Pople, *J. Chem. Phys.*, 1980, **72**, 650–654.
14 M. B. Goldfinger, K. B. Crawford and T. M. Swager, *J. Am. Chem. Soc.*, 1997, **119**, 4578–4593.
15 K. C. Moss, K. N. Bourdakos, V. Bhalla, K. T. Kamtekar, M. R. Bryce, M. A. Fox, H. L. Vaughan, F. B. Dias and A. P. Monkman, *J. Org. Chem.*, 2010, **75**, 6771–6781.
16 U. Rohr, P. Schlichting, A. Böhm, M. Gross, K. Meerholz, C. Bräuchle and K. Müllen, *Angew. Chem., Int. Ed.*, 1998, **37**, 1434–1437.
17 Recent examples: (*a*) K. Mitsudo, H. Sato, A. Yamasaki, N. Kamimoto, J. Goto, H. Mandai and S. Suga, *Org. Lett.*, 2015, **17**, 4858–4861; (*b*) Y.-Y. Lai, H.-H. Chang, Y.-Y. Lai, W.-W. Liang, C.-E. Tsai and Y.-J. Cheng, *Macromolecules*, 2015, **48**, 6994–7006; (*c*) J. W. Lim, S. H. Kim, J. Kim and J. N. Kim, *Bull. Korean Chem. Soc.*, 2015, **36**, 1351–1359; (*d*) Y.-L. Chen, J.-Y. Hsu, F.-Y. Lin, Y.-Y. Lai, H.-C. Chou and Y.-J. Cheng, *J. Org. Chem.*, 2016, **81**, 2534–2542.
18 Y. Wang and D. J. Burton, *Org. Lett.*, 2006, **8**, 5295–5298.
19 U. H. F. Bunz, V. Enkelmann, L. Kloppenburg, D. Jones, K. D. Shimizu, J. B. Claridge, H.-C. Loye and G. Lieser, *Chem. Mater.*, 1999, **11**, 1416–1424.
20 D. Sakamaki, D. Kumano, E. Yashima and S. Seki, *Chem. Commun.*, 2015, **51**, 17237–17240.
21 L. T. Scott, M. M. Hashemi and M. S. Bratcher, *J. Am. Chem. Soc.*, 1992, **114**, 1920–1921.
22 N. G. Connelly and W. E. Geiger, *Chem. Rev.*, 1996, **96**, 877–910.
23 I. Noviandri, K. N. Brown, D. S. Fleming, P. T. Gulyas, P. A. Lay, A. F. Masters and L. Phillips, *J. Phys. Chem. B*, 1999, **103**, 6713–6722.
24 C. M. Cardona, W. Li, A. E. Kaifer, D. Stockdale and G. C. Bazan, *Adv. Mater.*, 2011, **23**, 2367–2371.
25 M. Reig, J. Puigdollers and D. Velasco, *J. Mater. Chem. C*, 2015, **3**, 506–513.
26 H. Srour, T.-H. Doan, E. Da Silva, R. J. Whitby and B. Witulski, manuscript in preparation.
27 K. Ivaniuk, V. Cherpak, P. Stakhira, Z. Hotra, B. F. Minaev, G. V. Baryshnikov, E. Stromylo, D. Volyniuk, J. V. Grazulevicius, A. Lazauskas, S. Tamulevicius, B. Witulski, M. E. Light, P. Gawrys, R. J. Whitby, G. Wiosna-Sałyga and B. Luszczynska, *J. Phys. Chem. C*, 2016, **120**, 6206–6217.
28 Y. Yang, J. Liang, L. Hu, B. Zhang and W. Yang, *New J. Chem.*, 2015, **39**, 6513–6521.
29 M. R. Rao, A. Desmecht and D. F. Perepichka, *Chem. – Eur. J.*, 2015, **21**, 6193–6201.
30 B. S. Shaibu, S.-H. Lin, C.-Y. Lin, K.-T. Wong and R.-S. Liu, *J. Org. Chem.*, 2011, **76**, 1054–1061.
31 B. T. Haire, K. W. J. Heard, M. S. Little, A. V. S. Parry, J. Raftery, P. Quayle and S. G. Yeates, *Chem. – Eur. J.*, 2015, **21**, 9970–9974.

32 D. Volyniuk, V. Cherpak, P. Stakhira, B. F. Minaev, G. V. Baryshnikov, M. Chapran, A. Tomkeviciene, J. Keruckas and J. V. Grazulevicius, *J. Phys. Chem. C*, 2013, **117**, 22538–22544.
33 T. Tsutsui, Electroluminescence in Small Molecules, in *Organic Electroluminescence*, ed. Z. H. Kafafi, CRC Press, 2005, ch. 1, pp. 1–22.
34 C.-G. Zhan, J. A. Nichols and D. A. Dixon, *J. Phys. Chem. A*, 2003, **107**, 4184–4195.
35 (*a*) S. P. Jagtap, S. Mukhopadhyay, V. Coropceanu, G. L. Brizius, J.-L. Bredas and D. M. Collard, *J. Am. Chem. Soc.*, 2012, **134**, 7176–7185; (*b*) G. V. Baryshnikov, B. F. Minaev, V. A. Minaeva and V. G. Nenajdenko, *J. Mol. Model.*, 2013, **19**, 4511–4519.
36 A. Charaf-Eddin, T. Cauchy, F.-X. Felpin and D. Jacquemin, *RSC Adv.*, 2014, **4**, 55466–55472.
37 A. Tomkeviciene, J. V. Grazulevicius, K. Kazlauskas, A. Gruodis, S. Jursenas, T. H. Ke and C. C. Wu, *J. Phys. Chem. C*, 2011, **115**, 4887–4897.
38 J. Kalinowski, *Mater. Sci.-Pol.*, 2009, **27**, 735–756.
39 T. Mitani, T. Yamanaka, M. Suzui, T. Horigome, K. Hayakawa and I. Yamazaki, *J. Lumin.*, 1988, **39**, 313–322.
40 Y.-H. Lee, T.-C. Wu, C.-W. Liaw, T.-C. Wen, S.-W. Feng, J.-J. Lee, Y.-T. Wu and T.-F. Guo, *Org. Electron.*, 2013, **14**, 1064–1072.
41 R. Rimkus, S. Tumkevičius, T. Serevičius, R. Komskis, P. Adomėnas, A. Gruodis, V. Jankauskas, K. Kazlauskas and S. Juršėnas, *Dyes Pigm.*, 2016, **124**, 133–144.
42 X. Chen, C.-P. Kong, F.-Q. Bai and H.-X. Zhang, *J. Phys. Org. Chem.*, 2014, **27**, 973–980.
43 N. A. Kukhta, D. Volyniuk, J. V. Grazulevicius and J. Gytis, *J. Phys. Chem. C*, 2016, **120**, 1208–1217.
44 M. Grasruck, A. Schreiber, U. Hofmann, S. J. Zilker, A. Leopold, S. Schloter, C. Hohle, P. Stohriegl and D. Haarer, *Phys. Rev. B: Condens. Matter Mater. Phys.*, 1999, **60**, 16543–16548.
45 M. A. Khan, W. Xu, F. Wei, Y. Bai, X. Y. Jiang, Z. L. Zhang and W. Q. Zhu, *Solid State Commun.*, 2007, **144**, 343–346.
46 We fabricated spin-coated OLEDs from **3** but their performance was poor. The devices were assembled in the following configuration ITO/PVK:PBD + **3**(5%)/LiF/Al. The highest luminance was only 80 cd m^{-2} at 12 V. The turn on voltage was 9 V. The low performance was initially ascribed to the poor energy transfer from the host to the guest. Also in comparison to the vacuum-processed OLEDs described in the main text, the Al/LiF electrode has much higher work function and we did not use the ETL layer.
47 S. Reineke, M. Thomschke, B. L. Lüssem and K. Leo, *Rev. Mod. Phys.*, 2013, **85**, 1245.
48 J. Huang, J.-H. Su and H. Tian, *J. Mater. Chem.*, 2012, **22**, 10977–10989.
49 L. Duan, J. Qiao, Y. Sun, D. Zhang, G. Dong, L. Wang and Y. Qui, *Adv. Opt. Mater.*, 2013, **1**, 167–172.
50 Q. Xu, H. M. Duong, F. Wudl and Y. Yang, *Appl. Phys. Lett.*, 2004, **85**, 3357.
51 T. Higuchi, H. Nakanotani and C. Adachi, *Adv. Mater.*, 2015, **27**, 2019–2023.
52 (*a*) S.-A. Wang, W.-Y. Hung, Y.-H. Chen and K.-T. Wong, *Org. Electron.*, 2012, **13**, 1576–1582; (*b*) H.-H. Huang, D.-Y. Chua, P.-C. Kao and Y.-C. Chen, *Thin Solid Films*, 2008, **516**, 5669–5672; (*c*) D.-H. Lee, J. S. Choi, H. Chae, C.-H. Chung and S. M. Cho, *Curr. Appl. Phys.*, 2009, **9**, 161–164; (*d*) K.-L. Chen, *J. Nanomater.*, 2014, 173276.
53 L. Bao and M. D. Heagy, *Curr. Org. Chem.*, 2014, **18**, 740–772.
54 L. Wang, W.-Y. Wong, M.-F. Lin, W.-K. Wong, K.-W. Cheah, H.-L. Tamb and C. H. Chen, *J. Mater. Chem.*, 2008, **18**, 4529–4536.
55 J. Liang, S. Zhao, X.-F. Jiang, T. Guo, H.-L. Yip, L. Ying, F. Huang, W. Yang and Y. Cao, *ACS Appl. Mater. Interfaces*, 2016, **8**, 6164–6173.
56 S. Xue, X. Qiu, Q. Sun and W. Yang, *J. Mater. Chem. C*, 2016, **4**, 1568–1578.
57 (*a*) Y. Wang, W. Liu, L. Bu, J. Li, M. Zheng, D. Zhang, M. Sun, Y. Tao, S. Xuea and W. Yang, *J. Mater. Chem. C*, 2013, **1**, 856–862; (*b*) S. Xue, W. Liu, X. Qiu, Y. Gao and W. Yang, *J. Phys. Chem. C*, 2014, **118**, 18668–18675; (*c*) L. Bu, M. Sun, D. Zhang, W. Liu, Y. Wang, M. Zheng, S. Xue and W. Yang, *J. Mater. Chem. C*, 2013, **1**, 2028–2035.